Evaluation of a Modified Scheme for Shallow Convection: Implementation of CuP and Case Studies

LARRY K. BERG, WILLIAM I. GUSTAFSON JR., EVGUENI I. KASSIANOV, AND LIPING DENG

Pacific Northwest National Laboratory, Richland, Washington

(Manuscript received 3 May 2012, in final form 21 July 2012)

ABSTRACT

A new treatment for shallow clouds has been introduced into the Weather Research and Forecasting Model (WRF). The new scheme, called the cumulus potential (CuP) scheme, replaces the ad hoc trigger function used in the Kain–Fritsch cumulus parameterization with a trigger function related to the distribution of temperature and humidity in the convective boundary layer via probability density functions (PDFs). An additional modification to the default version of WRF is the computation of a cumulus cloud fraction based on the time scales relevant for shallow cumuli. Results from three case studies over the U.S. Department of Energy's Atmospheric Radiation Measurement (ARM) site in north-central Oklahoma are presented. These cases were selected because of the presence of shallow cumuli over the ARM site. The modified version of WRF does a much better job predicting the cloud fraction and the downwelling shortwave irradiance than control simulations utilizing the default Kain–Fritsch scheme. The modified scheme includes a number of additional free parameters, including the number and size of bins used to define the PDF, the minimum frequency of a bin within the PDF before that bin is considered for shallow clouds to form, and the critical cumulative frequency of bins required to trigger deep convection. A series of tests were undertaken to evaluate the sensitivity of the simulations to these parameters. Overall, the scheme was found to be relatively insensitive to each of the parameters.

1. Introduction and motivation

Shallow cumuli are quite common, occurring over large areas of the world's oceans and continents. These clouds play an important role in the earth's radiation budget by shading the surface. They have a smaller dynamic feedback on the environment than deeper clouds because of their limited horizontal and spatial extent and relatively small mass fluxes. Berg et al. (2011) documented the shortwave and longwave surface cloud radiative forcing associated with shallow cumuli at the U.S. Department of Energy's Atmospheric Radiation Measurement (ARM) Southern Great Plains Central Facility (referred to as the SGP) located in north-central Oklahoma. They found that the average shortwave surface forcing associated with shallow clouds was approximately -46 W m^{-2} over the summertime months. Their findings demonstrate that the proper treatment of shallow cumuli is important for accurate regional climate simulations or other applications, such as forecasting in support of the solar power industry, in which the accurate prediction of the downwelling irradiance is important.

A number of new parameterizations for shallow cumuli have been developed and implemented in various atmospheric models (e.g. Bretherton et al. 2004; Berg and Stull 2005; Neggers et al. 2009). As suggested by Bretherton et al. (2004), the parameterization problem can be broken into three parts: a binary trigger function used to indicate when there is convection (either shallow or deep) in the model grid column, a closure assumption that is used to represent the cloud-base mass flux, and a representation of cloud entrainment and detrainment to account for the exchange of mass between the cloud and its environment. The scheme of Bretherton et al. (2004) and Neggers et al. (2009) applies a critical value of vertical velocity to determine if shallow convection occurs. The cumulus potential (CuP) scheme developed by Berg and Stull (2005) uses a range of parcel buoyancies to initiate convection, and relates the cloud-base mass flux to the subgrid variability of temperature and humidity. Bretherton et al. (2004) used the distribution of vertical velocity to determine if convection occurs,

Corresponding author address: Larry K. Berg, P.O. Box 999, K9-30, Richland, WA 99352.
E-mail: larry.berg@pnl.gov

DOI: 10.1175/MWR-D-12-00136.1

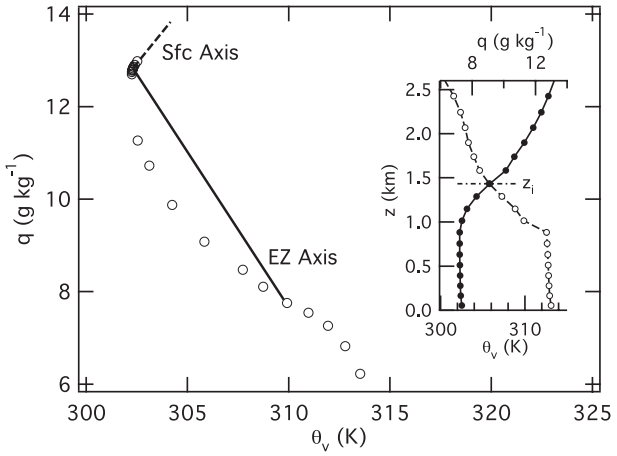

FIG. 1. Example of PDF fit parameters obtained from a WRF simulation valid at 1800 UTC on 2 Jul 2004. Circles indicate θ_v and q determined from the model grid column, the dashed line represents the surface axis (with slope S_{sfc}), and the solid line indicates the entrainment zone axis (with slope S_{ez}). For reference, the profiles of θ_v (solid) and q (broken), along with model-diagnosed boundary layer height (z_i), are shown in the inset panel.

which is in turn linked to the turbulence kinetic energy (TKE) predicted by the model. Neggers et al. (2009) also used the distribution of vertical velocity, along with several other boundary layer parameters, to predict the shallow clouds.

In addition to the prediction of the cloud-base mass flux, the scheme of Berg and Stull (2005) estimates the cloud fraction associated with shallow cumuli for inclusion in the radiation parameterization. In general, the cloud fraction and the cloud mass flux are not the same because active clouds with vigorous updrafts dominate the cloud mass flux and cloud fraction includes all cloud elements, even those decaying clouds without a strong updraft (e.g., Stull 1985). Berg and Stull (2005) derived a prognostic equation for the cloud fraction that is based on the distribution of temperature and humidity, an active cloud time scale that is based on the cloud height and updraft strength, and a cloud decay time scale that is a function of the thermodynamic properties of the cloud and the environment. Their expression is similar to those proposed by Albrecht (1981) and Haiden (1996). As will be shown later, the explicit treatment of cloud fraction yields better results when so-called empty clouds (predicted clouds that have no associated cloud liquid documented by Hannay et al. 2009) are simulated.

The methodology used to determine probability density functions (PDFs) of temperature and humidity is presented in section 2. It is shown that the size and shape of the PDF can be related to the boundary layer turbulence in a way that accounts for changes associated with the surface exchange of heat and moisture and entrainment mixing at the boundary layer top. Modification to the default version of the Weather Research and Forecasting Model (WRF) is described in section 3, with the modifications limited to alterations in the cumulus and radiation parameterizations. The data used for the validation of the improved schemes is presented in section 4. The data consist of a number of different observations and data products from the ARM SGP. The methodologies used in our analysis are presented in section 5, which includes a description of the WRF configuration, the selection of case-study days, and the sensitivity studies that were completed. The analysis and results are presented in section 6. The modified scheme is shown to do a better job predicting the formation of shallow convection and its impact on the surface energy budget. The new scheme is also shown to be relatively insensitive to new tunable parameters used in the modified parameterization.

2. Determination of PDFs of temperature and humidity

Berg and Stull (2004) developed a parameterization of PDFs of temperature and humidity by applying a mixing diagram approach that makes use of two axes: a surface axis and an entrainment zone axis. The slope of the surface axis is defined using jumps in virtual potential temperature (θ_v) and water vapor mixing ratio (q) between the surface and the boundary layer mean θ_v and q (represented by $\overline{\theta}_v$ and $\overline{q}$, respectively). The slope of the entrainment zone axis is defined using the difference between the $\overline{\theta}_v$ and $\overline{q}$ and the values of $\overline{\theta}_v$ and $\overline{q}$ in the free troposphere above the boundary layer. The spread of the PDF along each axis (σ_{sfc} and σ_{ez}, respectively) were defined in terms of standard boundary layer scales for temperature (θ_*) and humidity (q_*), which are defined as the ratio of the surface heat flux or moisture flux to the Deardorff convective velocity scale, respectively (e.g., Stull 1988).

There are some differences in the PDF parameterization presented by Berg and Stull (2004) and the scheme as it has been implemented in WRF. An example of the surface and entrainment zone slopes determined at a single grid point in a WRF simulation is shown in Fig. 1 (details of the simulation are described in section 5). In the WRF simulations, the slope of the surface axis (S_{sfc}) is defined in terms of the Bowen ratio, latent heat of evaporation, and the specific heat of air following Berg and Stull (2004), their Eq. (10), and is indicated by the broken line in the main part of Fig. 1. Determining the slope of the entrainment zone axis (S_{ez}) is more complicated. Two model levels are selected: one

located in the middle of the mixed layer and one two levels above the boundary layer top. In WRF, the model level that represents the boundary layer height (z_i) is diagnosed in the boundary layer parameterization. In the example shown in Fig. 1, z_i was diagnosed to be at grid level 12 and the boundary layer mean values are taken from grid level 6. The values of θ_v and q above the boundary layer are required to compute the jump of θ_v and q between the middle of the mixed layer and the entrainment zone. The model-predicted values from two levels above z_i are selected for these calculations. Selecting the model level immediately above z_i can lead to unstable behavior in cases in which the θ_v and q were not well mixed. Once the appropriate levels are determined, $S_{\rm ez}$ can be computed using

$$S_{\rm ez} = (\theta_{v,\rm ez} - \overline{\theta}_v)/(q_{\rm ez} - \overline{q}), \tag{1}$$

where $\theta_{v,\rm ez}$ and $q_{\rm ez}$ are the values two model levels above z_i. Some sensitivity to the particular model layer above z_i is that used to define $S_{\rm ez}$ is expected because of changes in the structure of the atmosphere above the boundary layer. As shown in their Fig. 3, Berg and Stull (2004) found that the thermodynamic state of air within the entrainment zone can be defined by the conditions near the middle of the mixed layer and at base of the free atmosphere. Thus, selecting a point very close the boundary layer top is most consistent with their results and should give the most realistic behavior of the PDF.

The standard deviations along both the surface and entrainment zone axes ($\sigma_{\rm sfc}$ and $\sigma_{\rm ez}$, respectively) are also needed to form the PDF. Berg and Stull (2004) defined expressions in terms of boundary layer scales θ_* and q_* that are determined using their Eq. (17). Rather than use the revised moisture scale, $q_{*,\rm new}$, proposed in their work, the standard form of q_* is used here, and it is assumed that the fit derived in Eq. (17b) of Berg and Stull (2004) can be used to describe the variation of $\sigma_{\rm sfc}/q_*$. One reason for making this change is that $q_{*,\rm new}$ requires the moisture flux at the boundary layer top while the standard value of q_* does not.

Once the values of $S_{\rm sfc}$, $S_{\rm ez}$, $\sigma_{\rm sfc}$, and $\sigma_{\rm ez}$ are determined the PDF of θ_v and q can be computed following Berg and Stull's Eqs. (4) and (5), which are repeated here

$$m = \frac{\theta_v - S_{\rm ez} q}{S_{\rm ez} - S_{\rm sfc}} \quad \text{and} \quad c = S_{\rm ez}\left(\frac{\theta_v - S_{\rm sfc} q}{S_{\rm ez} - S_{\rm sfc}}\right), \tag{2}$$

where m and c represent a new coordinate system projected onto the surface and entrainment zone axes (e.g., Schrieber et al. 1996; Berg and Stull 2004). The PDF is defined following Berg and Stull's Eq. (5),

$$f(m,c) = \frac{1}{2\pi\sigma_{\rm sfc}\sigma_{\rm ez}} \exp\left\{-\frac{1}{2}\left[\left(\frac{m}{\sigma_{\rm sfc}}\right)^2 - \left(\frac{c}{\sigma_{\rm ez}}\right)^2\right]\right\}, \tag{3}$$

where the values of σ_m and σ_c presented by Berg and Stull (2004) have been replaced by $\sigma_{\rm sfc}$ and $\sigma_{\rm ez}$, respectively.

3. Modifications to WRF

a. Modification of the convection parameterization

The Kain–Fritsch convective parameterization (Kain and Fritsch 1990; Kain 2004) is a commonly used option in the WRF for representing convection. The scheme applies an entraining/detraining cloud model to represent the transport of heat, moisture, and momentum by deep convective clouds. An ad hoc trigger function is applied to determine if convection initiates. The trigger function is defined to be a function of temperature, grid-resolved vertical velocity, and the depth over which the convection is assumed to occur.

Kain (2004) described a number of modifications to the original Kain–Fritsch parameterization. These changes include the addition of the representation of shallow, or nonprecipitating, convection. As part of this change, the cloud-base mass flux associated with shallow cumuli has been related to the TKE in the subcloud layer and the convective time scale τ_c [Kain's Eq. (9)]:

$$M_{u_0} = \left(\frac{\rm TKE_{MAX}}{k_0}\right)\left(\frac{m_{\rm USL}}{\tau_c}\right), \tag{4}$$

where $\rm TKE_{MAX}$ is the maximum value of TKE within the boundary layer, k_0 is a constant assumed to be 10 $\rm m^2\ s^{-2}$, and $m_{\rm USL}$ is the total mass within the updraft source layer. As the scheme is applied in versions 2 and 3 of WRF, $\rm TKE_{MAX}$ is assumed to be a constant value of 5, and τ_c is defined as a function of the horizontal grid spacing and wind speed at the lifting condensation level and at the approximate middle of the troposphere. As documented by Kain (2004), the value of τ_c is allowed to range from 1800 to 3600 s.

To implement CuP, a number of modifications have been made to the standard Kain–Fritsch scheme, including changing the trigger function, modifying the closure assumption related to the cloud-base mass flux, and changing the method used to estimate the cloud fraction when shallow convective clouds are present. These changes account for subgrid variability within the convective boundary layer in a more realistic way than is done in the default application of the scheme. Rather

than apply a single temperature perturbation, a range of values of θ_v and q determined from the PDF are used. These individual values of θ_v are also used to determine the range of possible parcel updraft speeds—one speed for each bin in the PDF. While this methodology is more time consuming than the standard application, depending on the number of bins used to represent the PDF, it allows for a more realistic treatment of subgrid variability of the shallow clouds by linking the clouds to the turbulence parameterization. Using the range of possible trigger perturbations within a given grid column, the Kain–Fritsch methodology is used to determine if deep convection occurs, shallow clouds form, or no clouds develop for each perturbation value. If deep convection is predicted by a sufficient number of bins of the PDF, then the single most likely perturbation pair of θ_v and q from the PDF that would lead to deep convection is used to calculate the resultant deep convective tendencies. This alternate methodology for deep convection is applied so that the treatment of deep convection in the Kain–Fritsch (KF)-CuP scheme is similar to the implementation of the standard Kain–Fritsch scheme. If no deep convection would trigger but one or more perturbation pairs would lead to shallow convection, each of these perturbation pairs are allowed to progress through the Kain–Fritsch shallow cumulus methodology, and the resulting tendencies are averaged together, as explained below.

The PDF of θ_v and q can be used to estimate the cloud mass flux. Kain (2004), his Eq. (9) can be modified to account for a distribution of air parcels associated with the PDF:

$$M_{u_0,i,j} = \left(\frac{\mathrm{TKE}_{\mathrm{MAX}}}{k_0}\right)\left(\frac{m_{\mathrm{USL}}}{\tau_c}\right)\alpha_{i,j}, \tag{5}$$

where $\alpha_{i,j}$ is the fraction of the PDF associated with the given potential temperature and mixing ratio for the ith and jth bin of the PDF. The total mass flux is determined by summing $M_{u_0,i,j}$ over the subset of parcels that rise and form clouds. Some parcels are either cooler than the environment and do not rise, or are sufficiently dry that they do not rise high enough to form clouds, so that the sum of $\alpha_{i,j}$ is generally less than 1.

Because of the range of perturbations used to trigger the scheme each time it is called, the modified version of the Kain–Fritsch scheme can predict a range of cloud properties (including cloud-base and cloud-top heights) within a given grid column because of the range of buoyancy and water vapor associated with the distribution of parcels. In this application, these variables are averaged together to yield a single estimate of the geometric properties of the shallow cumuli within the column. Since some perturbations are more likely, as determined by the PDF, the result from each perturbation is weighted by the perturbation probability when calculating the average. Future applications of the parameterization, such as accounting for three-dimensional radiative transfer, could make use of the subgrid variability of the clouds.

b. Modifications to the radiation parameterization

In preliminary simulations using both the default and modified schemes, we discovered numerous occasions in which shallow cumuli were predicted to form, but did not have an impact on the simulated surface radiation budget. This result was caused by the treatment of cloud fraction in WRF and the generation of so-called empty clouds (e.g., Hannay et al. 2009). For shallow cumuli, the amount of cloud water generated in the convective parameterization is generally small and the cloud water is evaporated within the cloud microphysics parameterization. This treatment can lead to cloud-free conditions within the radiation parameterization and no shortwave cloud effect in the surface radiation budget even when the cumulus parameterization is active. One way around this shortcoming is to introduce an alternative parameterization for the cloud fraction of convective clouds. In this case, the methodology derived by Berg and Stull (2005) is used to estimate the cloud fraction used by the radiation parameterization. In their scheme the cloud fraction is related to the fraction of rising parcels, the cloud water, and the thermodynamic structure of the cloud layer. One simplifying assumption for the equations derived by Berg and Stull (2005) is to assume that the cloud fraction associated with the population of cumuli does not change during the model time step, yielding a diagnostic equation

$$\alpha_{\mathrm{cloud}} = \tau_{\mathrm{cloud}}\frac{\alpha_{\mathrm{active}}}{t_{\mathrm{active}}}, \tag{6}$$

where τ_{cloud} is the cloud decay time scale, α_{active} is the fractional area of active clouds (equal to the area of the PDF of parcels that form clouds), and t_{active} is the time scale of active clouds, which is a function of the cloud-top height and the updraft strength ($t_{\mathrm{active}} = z_{\mathrm{top}}/w_*$). The value of τ_{cloud} is based on the integrated cloud water and saturation deficit:

$$\tau_{\mathrm{cloud}} = t_* \ln\left[1 + (1+\gamma)\frac{\int l_{\mathrm{cloud}}\,dz}{\int \delta q_s\,dz}\right], \tag{7}$$

where l_{cloud} is the integrated cloud water, δq_s is the saturation deficit ($q_{s,\mathrm{env}} - q_{\mathrm{env}}$), and $\gamma = (L/C_p)(\partial \overline{q}_{s,\mathrm{env}}/\partial \overline{T}_{\mathrm{env}})$. The radiation parameterization also

requires the cloud water content associated with the cloudy portion of the grid column. Thus, for instances with empty clouds, cumuli form but have no impact on the radiation budget since there is no explicit cloud water. In these cases, a representative value of 1 g kg^{-1} is assumed for the cloud water. This value was selected to be representative of boundary layer cumulus and is only used in the determination of the cloud optical depth.

4. Data sources

A number of different data sources are utilized to validate the performance of the WRF simulations. These datasets include measurements of the cloud macroscale properties, as well as the radiative forcing associated with shallow clouds. Berg and Kassianov (2008) compiled a climatology of cloud macroscale properties, including cloud-base height, cloud-top height, and cloud fraction at the SGP. Their climatology used an ARM data product produced using methods described by Clothiaux et al. (2000) that utilizes data collected by both a nadir-looking cloud radar and lidar to give the best possible estimate of cloud boundaries as a function of time. Similar datasets have also been used by Zhang and Klein (2010) to investigate the transition from shallow to deep convection at the SGP. Berg et al. (2011) derived the impact of shallow clouds on the surface radiation budget for the same site. Each of these studies used point observations made at the SGP. Fields of shallow clouds have a large amount of spatial and temporal inhomogeneity making comparisons with a point measure problematic, especially for case studies of limited duration. An additional gridded dataset that utilizes measurements of the downwelling all-sky direct and diffuse shortwave radiation to derive estimates of the fractional sky cover and downwelling clear-sky shortwave radiation around the ARM SGP site (Long and Ackerman 2000) has been utilized. This unique data product consists of clear- and all-sky irradiances as well as estimates of the fractional sky cover interpolated to a 0.5° × 0.5° grid using the methods of Caracena (1987) as described by Christy and Long (2003). Using this data product, the average downwelling shortwave radiation, as well as the fractional sky cover, was determined for concentric circles centered on the SGP with radii of 50 km.

The cloud fraction can be defined in a number of different ways. The fractional sky cover is the angular amount of the sky dome that is covered by clouds. For shallow cumuli near the horizon, this includes an influence from the cloud sides. The fractional sky cover can also be measured by a human observer on the ground or using a radiometric measurement with a large field of view. The earth cover is defined as the projection of the cloud area directly down to the surface. The earth cover is estimated from the time series of a nadir-looking narrow beam instrument (such as a fixed cloud radar or lidar) or a downward-looking satellite. The cloud fraction predicted by WRF is the earth cover, because it is linked to the fraction of the model grid box with clouds. In general, the fractional sky cover and the earth cover are not the same, with the fractional sky cover always being larger than the earth cover (Kassianov et al. 2005). However, the correlation between the two increases with averaging time. With these caveats in mind, the temporal and spatial averages of fractional sky cover will be compared directly with the earth cover predicted by WRF.

5. Methodology

Version 2.2 of WRF was configured with a single domain covering much of the central United States (Fig. 2). The grid consisted of 182 × 131 grid points in the horizontal with 12-km grid spacing and 45 vertical levels. The vertical resolution varied from approximately 120 m near the surface to nearly 1 km at the top of the domain. Boundary and initial conditions were obtained from the National Oceanic and Atmospheric Administration (NOAA)'s Global Forecast System (GFS) analysis that utilizes 1° resolution. The WRF single-moment (WSM) 6-class scheme was used to represent cloud microphysics (Hong and Lim 2006). The Community Atmospheric Model (CAM) longwave and shortwave radiation schemes were used to simulate the longwave and shortwave radiative transfer. The Mellor–Yamada–Janjić (Janjić 1990, 2002) boundary layer scheme was used, along with the Noah land surface model (Chen et al. 2007). The surface fluxes used in the simulations are taken directly from the Noah land surface scheme using input from the Eta Monin–Obukhov surface layer parameterization (Janjić 2002). Two different cumulus parameterizations were used: the standard Kain–Fritsch scheme (Kain and Fritsch 1990; Kain 2004) and the new KF-CuP scheme described in section 2. The simulations made using the standard KF scheme will be referred to as the control simulations, while the simulations made with the KF-CuP scheme will be called the experimental simulations. A positive-definite advection scheme was used in each set of simulations for all scalars, including moisture. Data from the cloud radar and lidar will be compared to values from the four WRF grid points surrounding the SGP, which are located 4.0, 8.5, 11, and 13 km away from the SGP.

a. Case studies

Using the methodology described by Berg and Kassianov (2008), there were a total of 19 days during

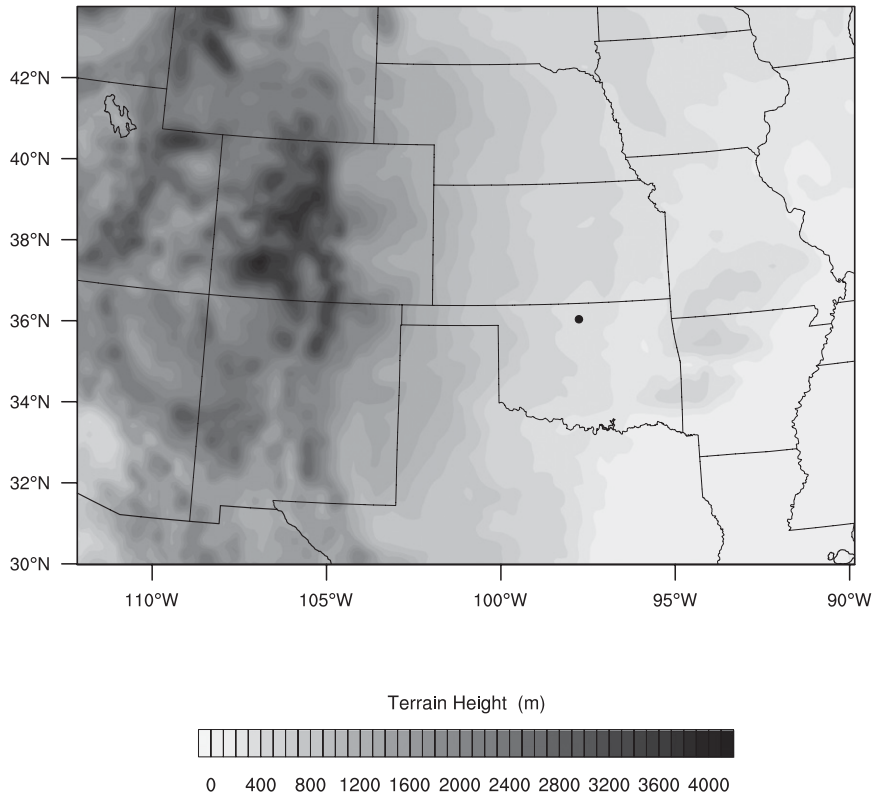

FIG. 2. Terrain height within the model domain used for this study. The black dot indicates the location of the ARM Southern Great Plains Central Facility.

which shallow cumuli and relatively small amounts of high clouds were observed at the SGP during the period May–August 2004. Of these 19 cases, three days were selected to serve as specific case studies for initial evaluation of the KF-CuP implemented in WRF: 16 May, 2 July, and 26 July. On 16 May, weather conditions over the Southern Great Plains were dominated by southerly flow, a stationary front stretching from Louisiana to Virginia, and a weak trough over eastern Colorado. In addition to shallow convection, a band of thin cirrus, associated with a disturbance aloft, was observed (Fig. 3). The total-sky imager (TSI) located at the SGP confirms the presence of shallow clouds throughout the day and the appearance of some high-level clouds late in the afternoon (Fig. 4). In contrast to the generally quiescent conditions observed on 16 May, 2 July is marked by the passage of a weak low pressure system and associated surface trough through the region of the SGP. These synoptic features are associated with a band of precipitation that passed over the SGP near 1000 UTC, which is still visible over eastern Kansas at 2000 UTC (Fig. 3). Shallow cumuli formed in the region behind the surface low-pressure center, and can be seen in the TSI images from the SGP (Fig. 4). On 26 July, the weather conditions over the region were dominated by a large area of high pressure reaching from Texas to Manitoba and the widespread occurrence of shallow cumuli (Fig. 3). Clouds were also present over the SGP (Fig. 4). Large amounts of cloudiness south of the SGP are associated with a stationary front located over southern Texas.

b. Sensitivity to new parameters

Four new tunable parameters have been added to WRF in conjunction with the KF-CuP scheme: 1) the number of PDF bins, 2) the size of the PDF bins, and 3) and 4) the threshold frequencies at which shallow and deep convection is assumed to occur. Values of the various parameters are listed in Table 1. Increasing the number of PDF bins while holding the bin size constant increases the magnitude of the largest perturbations of both virtual temperature and moisture. In their study of data collected during Boundary Layer Experiment 1996 (BLX96; Stull et al. 1997), Berg and Stull (2004) found that distributions of temperature and humidity were fairly narrow—on the order of 0.5 K for virtual temperature and 1 g kg^{-1} for water vapor mixing ratio. These distributions, however, were constructed from data that had been filtered to remove wavelengths longer than

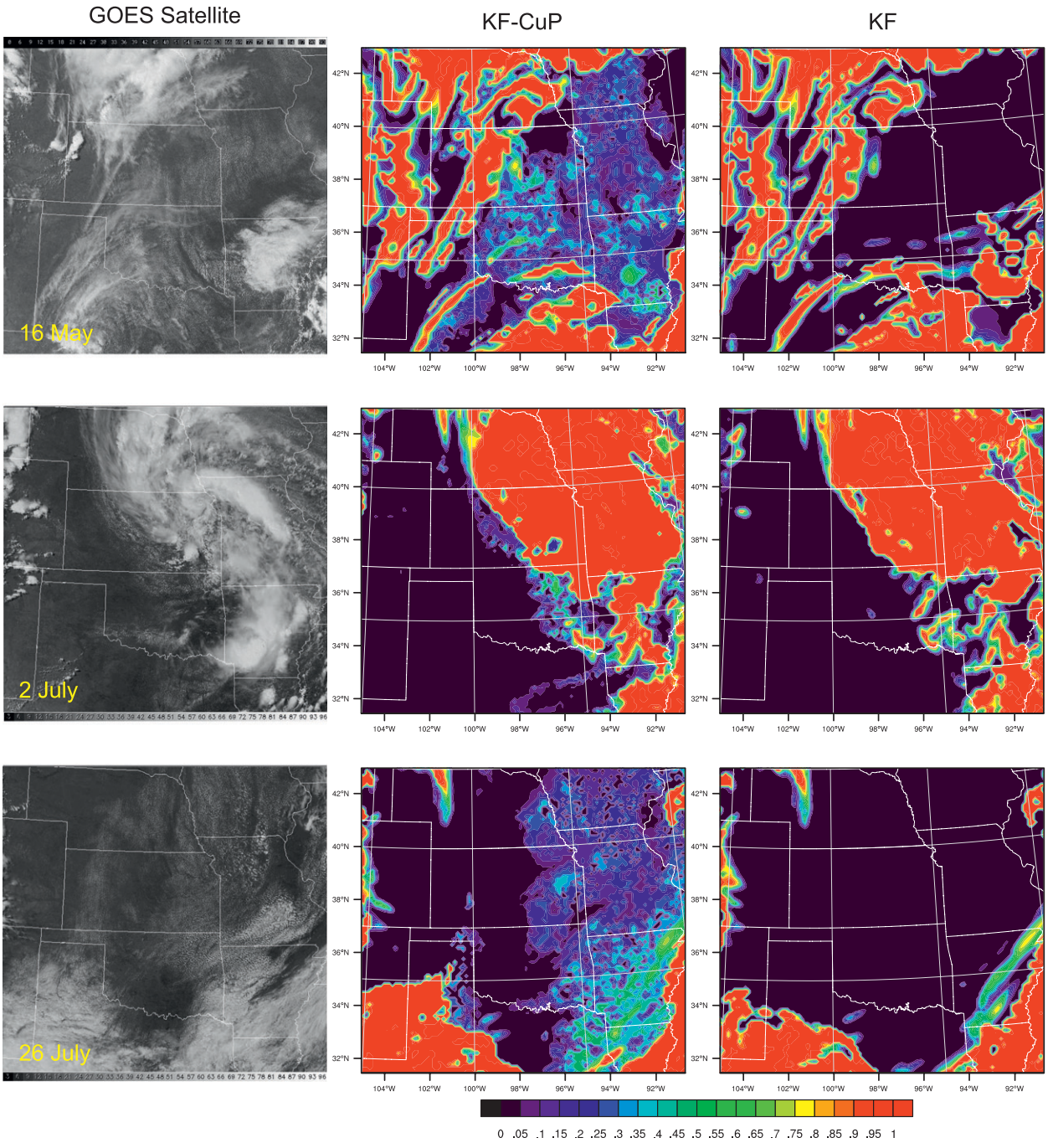

FIG. 3. (left) Satellite images valid at 2000 UTC [images courtesy of the National Center for Atmospheric Research (NCAR)] and WRF-simulated cloud fraction, assuming maximum cloud overlap, predicted using the (center) KF-CuP and (right) default KF at 2000 UTC on (top) 16 May, (middle) 2 Jul, and (bottom) 26 Jul.

5 km from the data. Over longer distances, the distributions showed more variation about the mean (e.g., Schrieber et al. 1996).

Simulations were completed for the three case-study days using PDFs with 121 (11 × 11), 441 (21 × 21), and 1681 (41 × 41) bins. In each of these tests the same bin size (0.1 K and 0.1 g kg^{-1}) were used. Increasing the number of bins increases the length of time needed to complete the simulations. Using 121, 441, or 1681 bins leads to a run time that is approximately 22%, 60%, or 90% longer, respectively, than the default configuration utilizing the standard KF scheme. For long-term

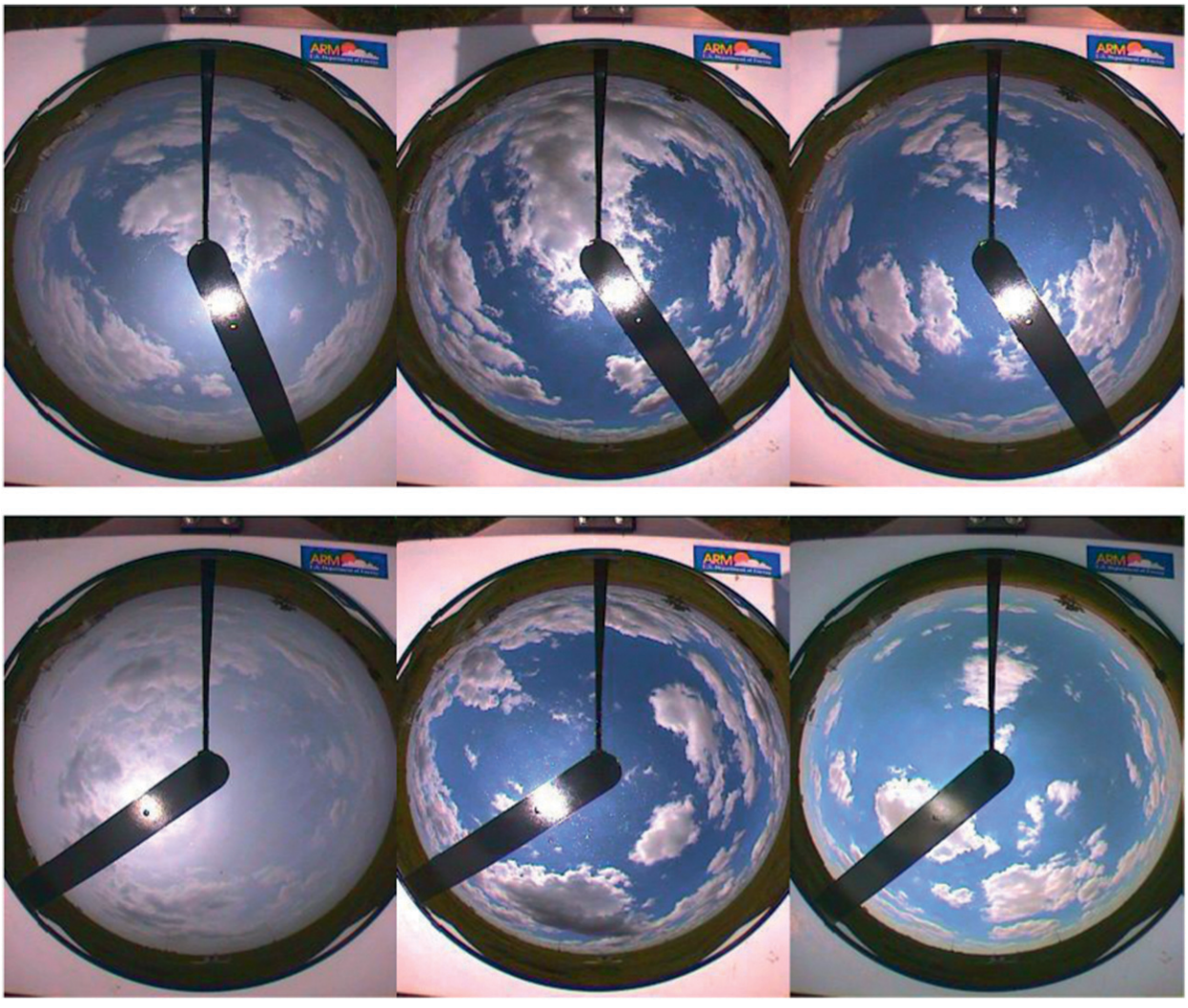

FIG. 4. Pictures from the total-sky imager located at the SGP at (top) 1800 and (bottom) 2000 on (left) 16 May, (center) 2 Jul, and (right) 26 Jul.

simulations, where model run time is paramount, methods of subsampling the PDF could be applied. One such method is Latin hypercube sampling, which has been used in microphysical parameterizations (Larson et al. 2005).

An additional set of simulations was completed using a PDF with 40 401 bins and a bin size of 0.01 K and 0.01 g kg^{-1}. This configuration was selected to investigate the impact of a very large number of bins as well as much smaller bin size. In this configuration the overall width of the PDF is 2 K and 2 g kg^{-1}, which is the same as the 441-bin configuration using bins 0.1 K and 0.1 g kg^{-1} in size. Decreasing the size of the PDF bins increases the resolution and provides more bins near the mean. This higher-resolution PDF may lead to an increase in the predicted cloud fraction because of this increase in resolution, but can lead to greater computational expense compared to a PDF spanning the same range with a smaller number of bins.

Another free parameter is the minimum frequency that a bin in the PDF represents before that bin is considered for shallow convection. The PDFs defined using Eq. (3) are for infinite ranges of temperature and moisture, but only a very small fraction of the PDF is far from the mean. In practice, it is undesirable to have a bin in the tail of the distribution contribute to the cloud properties. Therefore an additional check is applied, and

TABLE 1. Value of parameters used in various sensitivity studies.

Parameter	Values
Number of PDF bins	121, 441, 1681, 40 401
PDF bin size	0.1 K, 0.1 g kg^{-1}; 0.01 K, 0.01 g kg^{-1}
Minimum shallow frequency	0.1, 0.01, 0.001
Minimum deep frequency	0.1, 0.3, 0.5

TABLE 2. Bias in mean boundary layer potential temperature (θ) and q for selected case-study days. Bold type indicates smaller value.

	16 May 2004		2 Jul 2004		24 Jul 2004	
	1730	2330	1730	2330	1730	2330
θ (K)						
KF-CuP	−0.971	**0.178**	−2.975	−0.426	**0.319**	**0.048**
KF	**−0.859**	1.182	**−2.141**	**0.278**	0.415	0.577
q (g kg^{-1})						
KF-CuP	**1.473**	**0.992**	**0.043**	**1.168**	**0.336**	**0.966**
KF	1.519	1.419	0.415	1.486	0.682	1.345

if the frequency in a bin of the PDF is smaller than the critical value then that bin is ignored. A similar check is applied for deep convection, such that the cumulative frequency of bins in the PDF that trigger deep convection must meet or exceed some threshold before deep convection is considered.

6. Analysis and results

a. Case studies

For the case studies selected, the simulations made using the KF-CuP scheme generally predicted cooler and drier boundary layers than was predicted using the standard KF scheme (Fig. 5; Table 2). The differences between the KF and KF-CuP become more pronounced as the day progresses. This is consistent with a decrease of downwelling shortwave radiation at the surface (as well as a decrease in the surface sensible and latent heat fluxes) associated with increased cloud cover predicted by the KF-CuP scheme. Simulations completed using the KF scheme qualitatively underestimate the cloud fraction associated with shallow clouds (Fig. 3). The values shown in Fig. 3 show the cloud fraction in the column assuming maximum overlap. This methodology was selected for its simplicity and for easy qualitative comparison with the reflectivity shown in Fig. 3, and the large areas of red are associated with either thick clouds or areas of cirrus. In general, there is good correspondence between the areas with cloud fraction in Fig. 3 and the large areas of reflectivity shown in the figure. It is also clear from the results shown in Fig. 3 that the simulations completed using the KF parameterization significantly underestimate the area with partial cloud fraction, and generally predict clear conditions over the SGP. On the other hand, the KF-CuP scheme predicts large areas with cloud fraction less than 50%, which is consistent with visible satellite images shown in Fig. 4. Conditions on 2 July

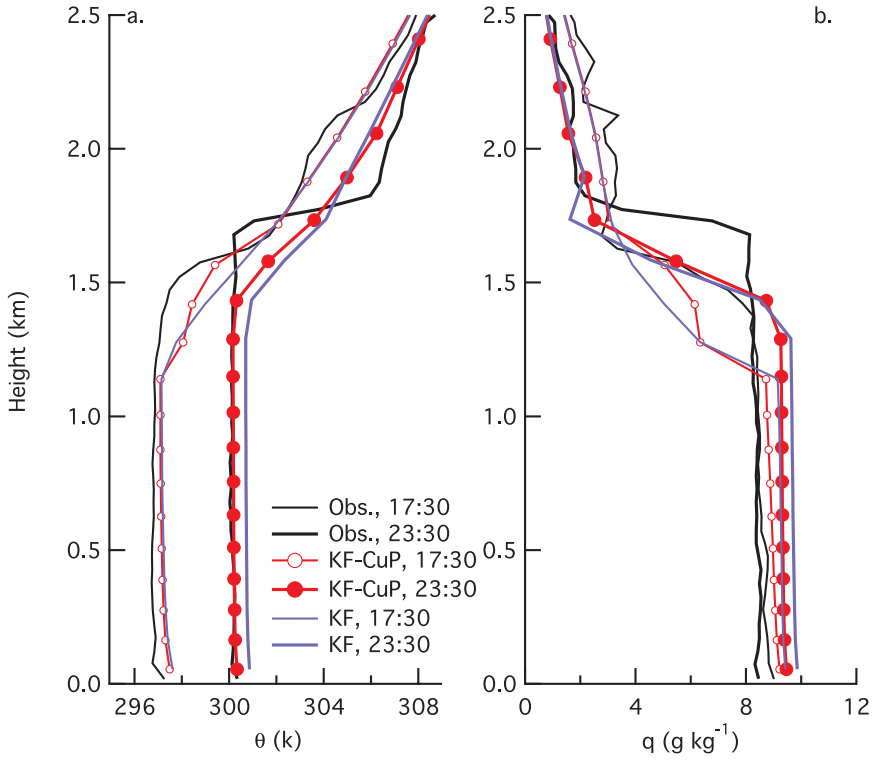

FIG. 5. Observed (black) and modeled KF (blue) and KF-CuP (red with symbols) profiles of (left) θ and (right) q for the grid point closest to the SGP at 1730 and 2330 UTC on 26 Jul.

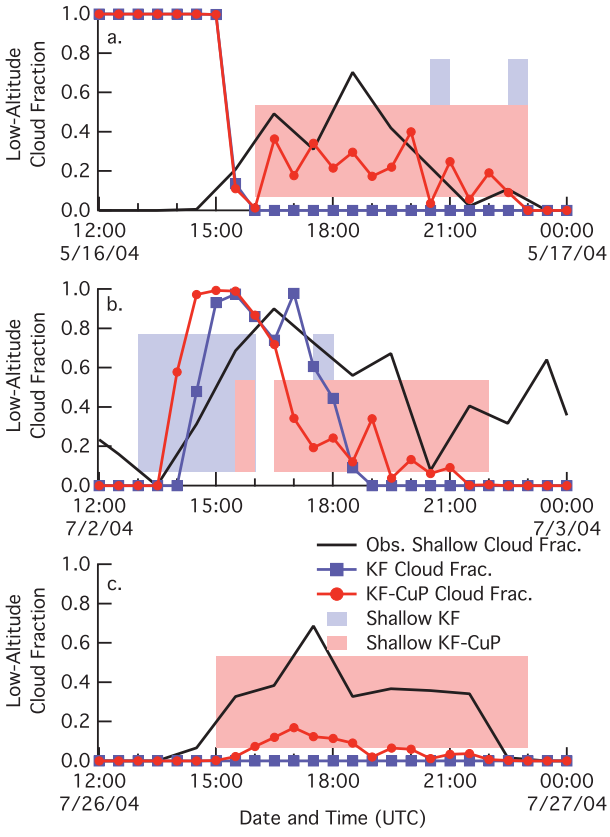

FIG. 6. Observed (black lines) and predicted low-altitude cloud fraction (defined as clouds occurring below 6 km) using the default KF (blue) and KF-CuP (red) for (a) 16 May, (b) 2 Jul, and (c) 26 Jul. Shading indicates periods during which the KF (blue) or KF-CuP (red) shallow convection parameterization is active.

are unique, with stronger synoptic forcing than the other case-study days. In this case both the KF and KF-CuP scheme underpredict the spatial extent of shallow clouds behind the front. However, the KF-CuP does a better job, predicting a larger amount of fractional cloudiness behind the front.

The simulated low-altitude cloud fraction (defined as any clouds below 6 km above ground level) can also be compared to the low-altitude cloud fraction derived from the cloud radar/lidar product computed using data collected from the SGP (Fig. 6). In this case, model results from the four WRF grid points closest to the SGP have been averaged together. The default version of the model generally underpredicts the cloud fraction compared to the observations derived from the cloud radar and lidar. The KF-CuP simulations do a better job, but still tend to underpredict the cloud fraction at the SGP (Fig. 6). The actual cloud fraction, however, can have a significant amount of spatial variability, as highlighted in the visible satellite images shown in Fig. 3. Simulations completed using both the KF and KF-CuP schemes predict low-altitude clouds from 1200 to 1500 UTC on 16 May, in contrast to the cloud fraction derived from the cloud radar and lidar that was 0 for the same period. These erroneously simulated clouds come from the explicit microphysics parameterization and are not associated with the cumulus parameterization. Once these clouds dissipate the default KF scheme predicts no clouds, while the KF-CuP scheme predicts significant amounts of clouds around the SGP. A similar behavior can be seen on 2 July, with both KF and KF-CuP predicting large amounts of clouds between 1400 and 1700 UTC. In this case, the early morning clouds are associated with the passage of the cold front. After 1800 UTC, the simulations completed with the standard KF scheme have very few clouds, while the KF-CuP maintains some shallow clouds until 2100 UTC. The default KF scheme predicts no clouds near the SGP on 26 July. During that same period the KF-CuP predicts some clouds, although still less than was observed by the cloud radar and lidar. Figure 6 also indicates periods during which the shallow cloud parameterization is active. The shallow convection is rarely active in the default KF scheme, and often has unrealistic timing, being applied in the early morning on 16 May and 2 July when shallow convection is expected to be less likely. In contrast the KF-CuP scheme is more active during the daylight hours.

The predicted cloud-base and cloud-top height can also be compared to values observed using the radar and lidar at the SGP. In general, the simulations completed using the KF-CuP scheme do a good job matching the observed minimum cloud-base height observed by the radar in each hour interval (Fig. 7). On 15 May and 2 July, there is good agreement between the observed and predicted cloud-base height. The KF-CuP predicts very shallow clouds on each of the days on both 16 May and 2 July compared to the small number of cloud-top height observations. Unfortunately, the radar- and lidar-derived cloud-top heights are missing during this period. This can happen in instances in which the radar is not working or is otherwise unable to determine the cloud-top height (e.g., during periods with insect contamination). The lidar gives a very accurate estimate of the cloud-base height, but can be attenuated by shallow cumuli and cannot be used to estimate the cloud-top height. The default scheme also predicts a much higher cloud top on 16 May than is seen with KF-CuP. On 26 July, the predicted cloud-base height is biased high by several hundred meters. As documented by Berg and Kassianov (2008), the base height of shallow cumuli is well predicted by the height of the lifting condensation level (z_{LCL}). The value of z_{LCL} is a function of the dewpoint depression, thus the bias in the cloud-base height can be attributed to a bias in the dewpoint depression and, hence z_{LCL}.

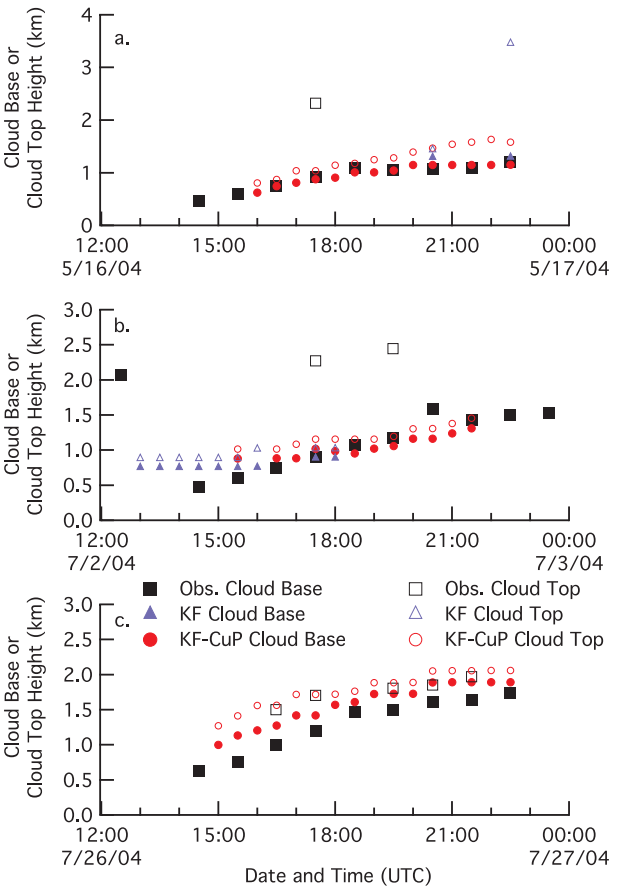

FIG. 7. Cloud-base height (filled symbols) and cloud-top height (open symbols) observed using the cloud radar and lidar (black) and simulated using KF-CuP (red) and the standard KF scheme (blue).

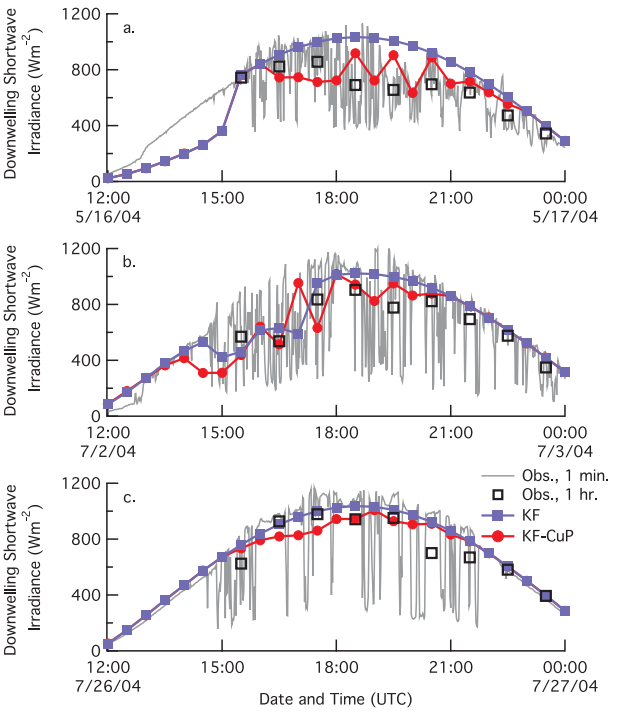

FIG. 8. Downwelling shortwave irradiance measured at the SGP averaged over a minute (gray lines) and 1 h (black squares) and predicted by KF-CuP (red) and the standard KF scheme (blue) on (a) 16 May, (b) 2 Jul, and (c) 26 Jul.

Consistent with the increased cloud fraction associated with simulations completed using KF-CuP, the downwelling shortwave surface irradiance is much closer to the observed 1-h averaged irradiance values than the results from the simulations completed using the KF scheme (Fig. 8). The simulations completed using the standard KF scheme had clouds between 2000 and 2100 as well as between 2200 and 2300 UTC on 16 May (indicted by the periods with cloud-base and cloud-top heights in Fig. 7). Because of issues in the parameterization of the cloud fraction, these clouds do not impact the simulated irradiance (note the smooth time series of downwelling irradiance for the KF scheme shown in Fig. 8). When fields of shallow cumuli are present, there can be large oscillations in the measured downwelling shortwave irradiance. Increased scattering of visible light can even lead to instances in which the all-sky downwelling irradiance is greater than the clear-sky value, especially over relatively short averaging times (e.g., Berg et al. 2011). Mesoscale models that apply 1D radiative transfer models are not able to capture this detail of the radiation field.

The simulations completed using both the KF and KF-CuP parameterizations can be compared to the gridded surface shortwave irradiance (described in section 4). In this case only model results and gridded estimates within 25 km of the SGP are used. With the exception of the early morning hours on 16 May and midmorning values on 2 July the KF scheme predicts clear skies (Fig. 9). On 16 May, both the KF and KF-CuP simulations predict fog in the vicinity of the SGP. In contrast, the observations from the TSI (not shown) as well as the observed gridded downward shortwave irradiance, indicate that conditions were clear. On 2 July, the KF and KF-CuP simulations both predict the existence of high-altitude clouds, which in this case is consistent with the observed cloud properties (Fig. 9) until 1900 UTC. One can also examine the variability of the irradiance over the 50-km diameter circle around the SGP. The error bars in Fig. 9 indicate the standard deviation over the area of interest. On 16 May, the observed shortwave irradiance is less variable than the WRF-CuP simulations, while on 2 July the variability simulated with WRF-CuP is nearly the same as that observed, and on 26 July the observed variability is larger.

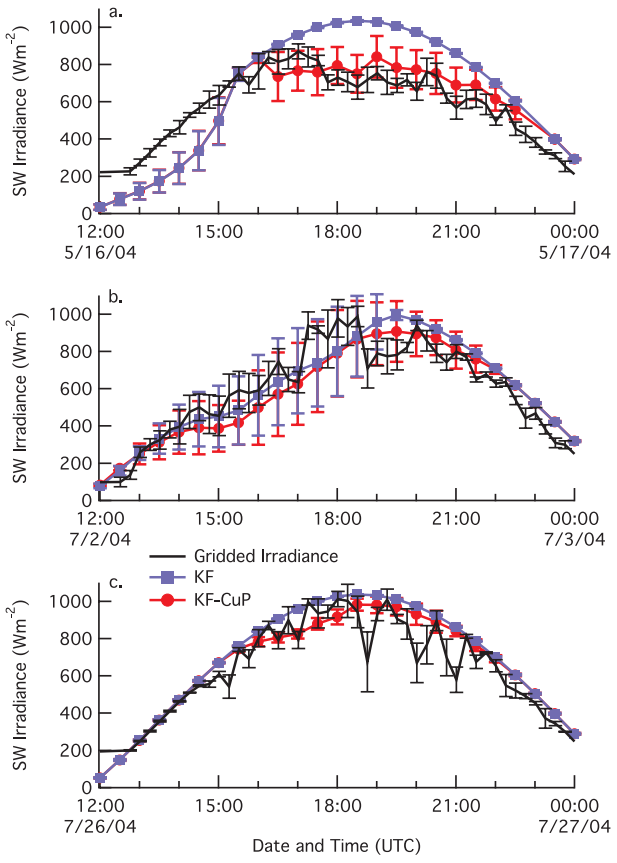

FIG. 9. Downwelling shortwave irradiance estimated using gridded data (black), and simulated using the KF (blue) and KF-CuP (red) parameterizations for a 50-km circle centered on the SGP on (a) 16 May, (b) 2 Jul, and (c) 26 Jul.

b. Sensitivity to new parameters

As described in sections 3 and 5, the KF-CuP scheme includes four new tunable parameters, including the number of bins used in the PDF, the relative size of the bins, and the minimum frequencies required for both shallow and deep convection. Tests were completed using PDFs with 121, 441, and 1681 bins for each variable (θ_v and q). In these tests the bin sizes were held constant at 0.1 K and 0.1 g kg^{-1}. The tests revealed that KF-CuP is not highly sensitive to the range of θ_v and q sampled by the PDF, as the predicted cloud fraction changed only slightly between the tests. The average cloud fraction associated with shallow clouds predicted by the KF-CuP scheme during the three case-study days (and only for periods during which clouds were simulated) was 0.15, 0.13, and 0.13 for simulations made using 121, 441, and 1681 bins, respectively. Another factor in the trend is the number of hours predicted to have clouds. There is some tendency for fewer hours with cloud cover when KF-CuP is used with 121 bins. The total number of hours with predicted clouds for the three case-study days was 16.5 h using 121 bins and 21 h using both 441 and 1681 bins, respectively. Simulations were also completed using 40 401 bins that were 0.01 K and 0.01 g kg^{-1} in size. The average cloud fraction for these simulations is 0.14—slightly more than was the case using 441 or 1681 larger bins. The number of hours with clouds using the 40 401 bins was also 21, just as was found using 441 or 1681 larger bins. Given the changes in the hours with clouds for simulations using 121 bins, the use of 441 or 1681 bins is recommended. The cloud-base height and cloud-top height were found to be insensitive to the number of bins and the bin size used (not shown).

Like the simulated cloud fraction, the downwelling irradiance is not a strong function of the number of bins or bin size that is used to define the PDF. The average downwelling irradiance at the surface was computed over all daylight hours (including periods with and without clouds) and ranged from 527 W m^{-2} for simulations using 121 bins to 525 W m^{-2} for simulations completed using 1681 bins. The average irradiance was slightly smaller, 517 W m^{-2}, for simulations made using the PDF represented by 40 401 smaller bins. As was found for the cloud fraction, there does not seem to be systematic changes in the amount of downwelling irradiance at the surface as a function of the bin choice.

Changing the minimum frequency required for a PDF bin to be included in the computation of the shallow clouds does not have an impact on the average cloud fraction, which was approximately 0.12 for minimum fractions of 10^{-1}, 10^{-2}, and 10^{-3}. When the minimum frequency is small, there are more hours with clouds (23 rather than 19 when using the larger minimum frequency). These extra hours tend to have very small cloud fractions, such that they tend to decrease the average cloud fraction a small amount. When these hours are not included, the cloud fraction computed using a minimum fraction of 10^{-3} increases to 0.14. Decreasing the minimum frequency also has some impact on the variability of the cloud fraction, with larger hour-to-hour variation in the cloud fraction associated with a smaller minimum frequency (not shown). This behavior, however, is more pronounced on some days than others. The simulated downwelling shortwave irradiance was found to be a weak function of the minimum frequency, with a slightly larger average value of 527 W m^{-2} for the cases when the minimum fraction is 10^{-1} compared to 534 W m^{-2} for a minimum fraction of 10^{-3}. Based on these results, use of a minimum fraction of 10^{-2} is recommended.

A set of simulations were completed with the minimum cumulative frequency required for the initiation of deep convection set to 0.1, 0.3, and 0.5. These particular values were selected to be representative of spatial

scales of deep convective clouds. At the 12-km horizontal grid spacing used here, one would expect that deep convective clouds would occupy a significant portion of the model grid box if convection is present. Changing the minimum cumulative frequency required for deep convection to occur between the three values has very little impact on the shallow cloud amounts predicted near the SGP, primarily because there are very few instances of deep convection near the SGP for the case-study days selected regardless of the threshold that was applied. For all three values of the minimum cumulative frequency required for deep convection the cloud fraction at the SGP is approximately 0.13. Likewise, there is very little difference in the amount of downwelling shortwave irradiance at the SGP, which is approximately 520 W m^{-2} for all three of the minimum frequencies. However, there are differences elsewhere in the domain where deep convection was more common, impacting the amount of precipitation associated with deep convection. The behavior of the KF-CuP scheme in respect to changes in the precipitation will be the subject of future work over the Southern Great Plains, as well as the overall sensitivity to horizontal resolution.

7. Summary

Two changes have been made to the standard WRF. First, a new method for representing the trigger function used in the KF scheme has been added. This new methodology accounts for the subgrid variability of temperature and humidity and generates a family of parcels used to trigger convection. The distribution defining the parcels is related to the turbulent mixing within the convective boundary layer. Second, a revised representation of subgrid convective cloud fraction has been added. This cloud fraction is used within the radiation parameterization to better account for the impact of shallow clouds on the surface energy budget.

Based on results from three case studies, the KF-CuP scheme is shown to do a better job predicting cloud fraction, cloud-base height, and the radiative impact of the clouds on the surface energy budget than the default KF scheme. These improvements could lead to significant improvement in climate simulations, where the radiative impact of shallow clouds would likely be most important. Both the KF-CuP and KF schemes underpredict the cloud-top height, but the number of times with reliable observations from the cloud radar is limited during the study period.

Four new parameters were added to WRF with the implementation of the KF-CuP scheme, including the number of bins in the PDF of temperature and humidity, the size of the respective bins, the minimum bin frequency required for inclusion, and the minimum fraction needed for the initiation of deep convection. Overall, the results were found to be relatively insensitive to the specific values of these parameters over a range of reasonable values. Recommended values of these parameters based on the simulations over the Southern Great Plains are 441 or 1681 bins that are 0.1 K and 0.1 g kg^{-1} in size, a minimum PDF frequency of 10^{-2} for the initiation of shallow convection, and a minimum cumulative frequency of 0.3 for the initiation of deep convection.

Because shallow cumuli produce little rain and have a small convective mass flux, and do not mix the column of air as effectively as deep cumuli, shallow cumuli have not received as much attention in atmospheric models. However, as is shown here, improvement in the handling of shallow cumuli leads to improved energy partitioning in the model. Short-term simulations, such as those done for weather forecasting, would not show vast differences in their results because of these modifications because the improved forecast of downwelling shortwave radiation would take time to feedback to other variables such as surface temperature and precipitation. However, the improvements are more important for climate models that must maintain proper energy balance over longer time frames. Using the CuP approach should significantly improve climate simulations.

Acknowledgments. We thank Dr. Richard Easter for numerous discussions related to this work and Dr. Minghuai Wang for his careful review of an earlier version of the manuscript. This work has been supported by the Office of Biological and Environmental Research (OBER) of the U.S. Department of Energy (DOE) as part of the Atmospheric Radiation Measurement (ARM) and Atmospheric System Research (ASR) Programs. The Pacific Northwest National Laboratory (PNNL) is operated by Battelle for the DOE under Contract DE-A06-76RLO 1830. A portion of the research was performed using PNNL Institutional Computing.

REFERENCES

Albrecht, B. A., 1981: Parameterization of trade-cumulus cloud amounts. *J. Atmos. Sci.,* **38,** 97–105.

Berg, L. K., and R. B. Stull, 2004: Parameterization of joint frequency distributions of potential temperature and water vapor mixing ratio in the daytime convective boundary layer. *J. Atmos. Sci.,* **61,** 813–828.

——, and ——, 2005: A simple parameterization coupling the convective daytime boundary layer and fair-weather cumuli. *J. Atmos. Sci.,* **62,** 1976–1988.

——, and E. I. Kassianov, 2008: Temporal variability of fair-weather cumulus statistics at the ACRF SGP site. *J. Climate,* **21,** 3344–3358.

——, ——, C. N. Long, and D. L. Mills Jr., 2011: Surface summertime radiative forcing by shallow cumuli at the Atmospheric

Radiation Measurement Southern Great Plains site. *J. Geophys. Res.,* **116,** D01202, doi:10.1029/2010JD014593.

Bretherton, C. S., J. R. McCaa, and H. Grenier, 2004: A new parameterization for shallow cumulus convection and its application to marine subtropical cloud-topped boundary layers. Part I: Description and 1D results. *Mon. Wea. Rev.,* **132,** 864–882.

Caracena, F., 1987: Analytic approximation of discrete field samples with weighted sums and the gridless computation of field derivatives. *J. Atmos. Sci.,* **44,** 3753–3768.

Chen, F., and Coauthors, 2007: Description and evaluation of the characteristics of the NCAR high-resolution land data assimilation system. *J. Appl. Meteor. Climatol.,* **46,** 694–713.

Christy, J. E., and C. N. Long, 2003: Surface cloud grid (SfcCldGrid) value-added product: Algorithm operational details and explanations. Atmospheric Radiation Measurment Program ARM-TR-010, 20 pp.

Clothiaux, E. E., T. P. Ackerman, G. G. Mace, K. P. Moran, R. T. Marchand, M. A. Miller, and B. E. Martner, 2000: Objective determination of cloud heights and radar reflectivities using a combination of active remote sensors at the ARM CART sites. *J. Appl. Meteor.,* **39,** 645–665.

Haiden, T., 1996: Generalization of Albrecht's cumulus cloud amount parameterization. *J. Atmos. Sci.,* **53,** 3164–3167.

Hannay, C., D. L. Williamson, J. J. Hack, J. T. Kiehl, J. G. Olson, S. A. Klein, C. S. Bretherton, and M. Köhler, 2009: Evaluation of forecasted southeast Pacific stratocumulus in the NCAR, GFDL, and ECMWF models. *J. Climate,* **22,** 2871–2889.

Hong, S. Y., and J. O. J. Lim, 2006: The WRF Single-Moment 6-class microphysics scheme (WSM6). *J. Korean Meteor. Soc.,* **42,** 129–151.

Janjić, Z. I., 1990: The step-mountain coordinate: Physical package. *Mon. Wea. Rev.,* **118,** 1429–1443.

——, 2002: Nonsingular Implementation of the Mellor-Yamada Level 2.5 scheme in the NCEP Meso model. NCEP Office Note 437, 61 pp.

Kain, J. S., 2004: The Kain–Fritsch convective parameterization: An update. *J. Appl. Meteor.,* **43,** 170–181.

——, and J. M. Fritsch, 1990: A one-dimensional entraining/detraining plume model and its application in convective parameterization. *J. Atmos. Sci.,* **47,** 2784–2802.

Kassianov, E., C. N. Long, and M. Ovtchinnikov, 2005: Cloud sky cover versus cloud fraction: Whole-sky simulations and observations. *J. Appl. Meteor.,* **44,** 86–98.

Larson, V. E., J.-C. Golaz, H. Jiang, and W. R. Cotton, 2005: Supplying local microphysics parameterizations with information about subgrid variability: Latin hypercube sampling. *J. Atmos. Sci.,* **62,** 4010–4026.

Long, C. N., and T. P. Ackerman, 2000: Identification of clear skies from broadband pyranometer measurements and calculation of downwelling shortwave cloud effects. *J. Geophys. Res.,* **105** (D12), 15 609–15 626.

Neggers, R. A. J., M. Köhler, and A. C. M. Beljaars, 2009: A dual mass flux framework for boundary layer convection. Part I: Transport. *J. Atmos. Sci.,* **66,** 1465–1487.

Schrieber, K., R. Stull, and Q. Zhang, 1996: Distributions of surface-layer buoyancy versus lifting condensation level over a heterogeneous land surface. *J. Atmos. Sci.,* **53,** 1086–1107.

Stull, R. B., 1985: A fair-weather cumulus cloud classification scheme for mixed-layer studies. *J. Climate Appl. Meteor.,* **24,** 49–56.

——, 1988: *An Introduction to Boundary Layer Meteorology.* Kluwer Academic Publishers, 666 pp.

——, E. Santoso, L. Berg, and J. Hacker, 1997: Boundary Layer Experiment 1996 (BLX96). *Bull. Amer. Meteor. Soc.,* **78,** 1149–1158.

Zhang, Y., and S. A. Klein, 2010: Mechanisms affecting the transition from shallow to deep convection over land: Inferences from observations of the diurnal cycle collected at the ARM Southern Great Plains site. *J. Atmos. Sci.,* **67,** 2943–2959.